3D unsteady computations of evaporative instabilities in a sessile drop of ethanol on a heated substrate

Sergey Semenov,[1,2] Florian Carle,[1,3] Marc Medale,[1] and David Brutin[1,4,a]

[1]*Aix-Marseille University, IUSTI UMR 7343 CNRS, 13453 Marseille, France*
[2]*Aix-Marseille University, MADIREL UMR 7246 CNRS, 13013 Marseille, France*
[3]*Yale Quantum Institute, Yale University, New Haven, Connecticut 06511, USA*
[4]*Institut Universitaire de France, 75231 Paris, France*

Droplets are ubiquitous and have been studied for a century; however, their internal flow pattern and related instabilities that occur in the course of evaporation are not fully understood yet. In this paper, we report our investigation results on an ethanol drop evaporating onto a heated substrate under weightlessness conditions and with a pinned contact line. They have been obtained from both experiments and 3D unsteady computations in order to determine what kind of instabilities develop. Our one-sided model demonstrates quantitative agreement with experiments and confirms that experimentally observed instabilities are driven by thermo-capillary stress and not by the gas convection. Post-processed infrared images drawn from computations led us to conclude that the experimentally observed thermo-convective instabilities, which look very similar to hydrothermal waves in the infrared spectrum, are actually nothing else than unsteady Benard-Marangoni instabilities. *Published by AIP Publishing.* https://doi.org/10.1063/1.5006707

Evaporating sessile drops of various liquids are widely encountered in nature and have plenty of industrial and bio-medical applications: heat exchangers,[1] nanoparticle deposition (coffee-ring effect),[2] spraying of herbicides and pesticides on hydrophobic leaves,[3] inkjet printing,[4,5] and blood analysis.[6–8] As a result, evaporating sessile drops constitute an interest for both academic and industry communities. This problem is rich with numerous physical phenomena: diffusive and convective vapour transport, kinetics of vapour molecule transfer across the liquid-gas interface (Hertz-Knudsen-Langmuir equation), evaporative interface cooling, radiative heat transfer, Marangoni flows and instabilities, particle sedimentation and deposition, adsorption of chemicals on interfaces, adsorbed precursor films, contact line instabilities, and pinning/depinning processes. Many of these phenomena can be visualized with the aid of modern optical instruments. For example, the field of vapour concentration around the droplet can be observed with the aid of digital holographic interferometry.[9] Observations of the infrared (IR) spectrum give visual information about thermal processes in a droplet[10–15] and allow estimating of the temperature field on its surface.[15–18] Among all observable phenomena, a particular interest has been given to one particular type of spontaneously developing thermo-capillary instabilities, formerly reported as hydrothermal waves (HTWs). Conventional HTWs are observed in thin liquid layers whose surface is subject to a lateral temperature gradient.[19–23] In sessile droplets, however, evaporation induces naturally such temperature gradients, leading to fascinating thermo-convective instabilities, as observed in the IR spectrum of volatile liquids (methanol, ethanol, and FC-72) on heated substrates by Sefiane *et al.*[10] and later by few other researchers.[13–15,17]

However, it is still not clear what is exactly observed in sessile droplets: is it hydrothermal waves or unsteady Benard-Marangoni (BM) instabilities or a combination of both? In order to answer this question, it is necessary to understand underlying hydrodynamics and heat transfer since according to Smith and Davis[19,20] [see also Ref. 24 and p. 115 in Ref. 25], HTWs are distinguished from other thermo-capillary instabilities by the following attributes: they appear only as a secondary unsteady thermo-convective instability in a basic shear flow (primary thermo-capillary flow) directed along the longitudinal temperature gradient at the liquid surface; the mechanism of HTWs propagation does not require any deflection of the free surface of the liquid layer.

The purpose of this communication is to unveil by means of direct numerical simulations the proper sequence of instabilities that enter into play and to determine the underlying triggering mechanism. Indeed, it turns out that the unsteady Benard-Marangoni instability is in fact the triggering instability in the considered case; meanwhile, hydrothermal waves are the consequence of the former instability to distribute over the interface the time evolving thermo-convective cells. The presented computations fully reproduce experimentally observed patterns. Therefore, the authors think that it is important to deliver to the scientific community the idea that in sessile drop evaporation, the observed instabilities should not systematically be associated only with HTWs since they are not generally the triggering mechanism. In the present work, we address this question related to the nature of instabilities that develop during sessile droplet evaporation of volatile liquids (HTWs or BM instabilities?). A one-sided numerical model has been developed to compute 3D unsteady and coupled hydrodynamics and heat transfers in a sessile drop of ethanol on a heated substrate. We assume a pinned contact line and a spherical-cap

[a]Author to whom correspondence should be addressed: david.brutin@univ-amu.fr

shape of the liquid-gas interface. The computed temperature field is used for post-processing of top-view IR images of a semi-transparent droplet (in the IR spectrum), which enabled us to validate our model against experimental IR images. Our computations contribute to figure out the internal 3D flow structure in the droplet and also to determine the driving mechanism and energy sources of the observed thermo-convective instability and thus clarify its nature. A Cartesian system of coordinates (x, y, z) is used, with its origin being located at the geometrical center of the droplet-substrate contact area and the z-axis directed perpendicular to the liquid-solid interface pointing upwards. Let $\hat{\mathbf{x}}$, $\hat{\mathbf{y}}$ and $\hat{\mathbf{z}}$ be the constant unit vectors in directions of x, y, and z axes, respectively. A semi-analytical formula has been previously developed to model the mass flow rate J (in kg s^{-1}) of unsteady diffusion-limited evaporation for a non-isothermal pinned sessile droplet while accounting for Stefan flow in the gas.[26] It reads

$$J^{Stefan}(L,T_{av},\theta(t),t) = 2\pi D_{eff}^* L F(\theta(t))$$
$$\times \left(1 + \frac{LF(\theta(t))}{\sqrt{\pi D_{eff}^* t}}\right)\rho_g^* \ln\left(\frac{\rho_g^* - \rho_{v,\infty}}{\rho_g^* - \rho_{v,sat}^*}\right), \quad (1)$$

where

$$D_{eff}^* = A\sqrt{T_{av}T_\infty}\left(\sqrt{T_{av}} + \sqrt{T_\infty}\right)/2, \quad (2)$$

$$A = (Dp_g)_{ref}/\left(p_g T_{ref}^{3/2}\right), \quad (3)$$

$$T_{av} = \frac{1}{\Gamma}\int_\Gamma T d\Gamma, \quad (4)$$

$$\rho_g^* = p_g M_g^*/(RT_{av}), \quad (5)$$

$$F(\theta) = \begin{cases} (0.6366\,\theta + 0.09591\,\theta^2 - 0.06144\,\theta^3)/\sin\theta \\ \quad \text{for } 0 \leq \theta < \pi/18, \\ (0.00008957 + 0.6333\,\theta + 0.116\,\theta^2 - 0.08878\,\theta^3 \\ \quad + 0.01033\,\theta^4)/\sin\theta \quad \text{for } \pi/18 \leq \theta \leq \pi, \end{cases}$$
$$(6)$$

$$\rho_{v,sat}(T) = \frac{p_{v,sat}^{ref} M_v}{RT}\exp\left[-\frac{\Lambda^*}{R}\left(\frac{1}{T} - \frac{1}{T_{sat}^{ref}}\right)\right], \quad (7)$$

$$\rho_{v,sat}^* = \rho_{v,sat}(T_{av}). \quad (8)$$

L is the droplet radius, T_{av} and T_∞ are the corresponding average temperature of the liquid-gas interface Γ [see Eq. (4)] and the ambient one, respectively, t is the time, $\theta(t)$ is the time-dependent contact angle, $F(\theta)$ is the function of the contact angle, derived by Picknett and Bexon[27] and equivalent to the one derived later by Popov,[28] the asterisk stands for a dependence on T_{av}, D_{eff}^* is the effective diffusion coefficient for vapour in ambient gas, p_g is the ambient gas pressure, $(Dp_g)_{ref} = 1.337$ Pa m^2 s^{-1} at $T_{ref} = 298$ K for ethanol vapour in air,[29] ρ_g^* [see Eq. (5)] and $M_g^* = M_{air}(1 - X_v^*) + M_v X_v^*$ are the corresponding density and molar mass of the gas at Γ,

where M_{air} and M_v are molar masses of the corresponding air and vapour (0.046 kg/mol for ethanol) and $X_v^* = \rho_{v,sat}^* RT_{av}/(M_v p_g)$ is the vapour molar fraction, $\rho_{v,sat}(T)$ is the local saturated vapour density at Γ [Clausius-Clapeyron equation, see Eq. (7)], R is the universal gas constant, $\Lambda^* = c_1(1 - T_{av}/T_c)^{c_2}$ is the latent heat of vaporization with $c_1 = 55789$ J/mol, $c_2 = 0.31245$, and $T_c = 514$ K for ethanol, $p_{v,sat}^{ref} = 13838$ Pa at $T_{sat}^{ref} = 308.15$ K, and $\rho_{v,\infty}$ is the vapour density in the ambient gas far away from the droplet. Equation (1) has been used in a two-parametric approximation, j_{approx}, for a non-isothermal vapour flux distribution along the droplet surface (see Ref. 26)

$$j_{approx} = j_i^*(r,\theta)[1 + B(T - T_{av})] + \Delta h\nabla_\Gamma \cdot \mathbf{j}_\tau, \quad (9)$$

where $r = \sqrt{x^2 + y^2}$ and

$$\mathbf{j}_\tau = -D(T)\nabla_\Gamma\rho_{v,sat}(T) + \rho_{v,sat}(T)\mathbf{u}_\tau. \quad (10)$$

B and Δh are two parameters, $\nabla = \hat{\mathbf{x}}\frac{\partial}{\partial x} + \hat{\mathbf{y}}\frac{\partial}{\partial y} + \hat{\mathbf{z}}\frac{\partial}{\partial z}$ is the nabla-operator, $\nabla_\Gamma = (\mathbf{I} - \mathbf{nn})\cdot\nabla$, where $\mathbf{I}$ is the identity tensor and $\mathbf{n}$ is the unit normal vector at the liquid-gas interface pointing into the gas phase, $\mathbf{j}_\tau$ is the tangential component of the vapour flux [see Eq. (10)], $D(T) = AT^{3/2}$ is the local diffusion coefficient, $\mathbf{u}_\tau = (\mathbf{I} - \mathbf{nn})\cdot\mathbf{u}$ is the tangential component of the velocity vector, $\rho_{v,sat}(T)$ is the local saturated vapour density, $\nabla_\Gamma \cdot \mathbf{j}_\tau$ is a surficial divergence [see Eq. (22)] of the surficial vector $\mathbf{j}_\tau$, and finally, $j_i^*(r,\theta)$ is an isothermal version of the vapour flux distribution along the droplet surface:

$$j_i^*(r,\theta) = j_0^*\chi^{-\lambda}(1 - \omega)$$
$$\text{for } 0 \leq \theta \leq \pi/2 \quad \text{and} \quad 0 \leq r < L, \quad (11)$$

where

$$j_0^* = \frac{J^{Stefan}(L,T_{av},\theta(t),t)G(\theta)}{2\pi L^2 F(\theta)}, \quad (12)$$

$$G(\theta) = 0.008348\,\theta^4 - 0.1026\,\theta^3$$
$$+ 0.001815\,\theta^2 + 0.4491\,\theta + 0.6368, \quad (13)$$

$$\chi = 1 - (r/L)^2, \quad (14)$$

$$\lambda = (\pi - 2\theta)/(2\pi - 2\theta), \quad (15)$$

$$\omega = \begin{cases} H\left[3 - \sqrt{4 + 5(1 - \theta/\theta_{HE})^2}\right], \\ \quad 0 \leq \theta \leq \theta_{HE} \\ -E + \sqrt{\lambda_E^2 E^2 + (1 - \lambda_E^2)(H + E)^2}, \\ \quad \theta_{HE} < \theta \leq \pi/2 \end{cases}, \quad (16)$$

$$\lambda_E = (2\theta - 2\theta_{HE})/(\pi - 2\theta_{HE}), \quad (17)$$

$$\theta_{HE} = 0.7864\,H + 0.9103, \quad (18)$$

$$E = -2.679\,H + 0.7265, \quad (19)$$

$$H = 0.26(1 - \chi^{0.7}). \quad (20)$$

Defining the liquid-gas interface $\Gamma : z = f(x,y)$, we can represent $\mathbf{j}_\tau$ as a function $\mathbf{v}$ of only two coordinates

$$\mathbf{j}_\tau(x,y,z) = \mathbf{j}_\tau\big(x,y,f(x,y)\big) \equiv \mathbf{v}(x,y). \qquad (21)$$

Then, provided that $n_z \neq 0$, term $\mathbf{V}_\Gamma \cdot \mathbf{j}_\tau$ in Eq. (9) can be expressed as

$$\mathbf{V}_\Gamma \cdot \mathbf{j}_\tau = \mathbf{a} \cdot (\mathbf{v})'_x + \mathbf{b} \cdot (\mathbf{v})'_y, \qquad (22)$$

where symbols $(\cdot)'_x$ and $(\cdot)'_y$ denote partial derivatives with respect to x and y, and vectors $\mathbf{a}$ and $\mathbf{b}$ are given as follows:

$$\begin{aligned}\mathbf{a} &= (\mathbf{I} - \mathbf{nn}) \cdot \hat{\mathbf{x}} = (1 - n_x^2, \ -n_x n_y, \ -n_x n_z), \\ \mathbf{b} &= (\mathbf{I} - \mathbf{nn}) \cdot \hat{\mathbf{y}} = (-n_y n_x, \ 1 - n_y^2, \ -n_y n_z),\end{aligned} \qquad (23)$$

with $n_x = -f'_x n_z$, $n_y = -f'_y n_z$ and $n_z = \frac{1}{\sqrt{1 + (f'_x)^2 + (f'_y)^2}}$ being the components of the normal vector $\mathbf{n}$. Expression (22) has been implemented in our numerical model along with Eq. (9) as a boundary condition for the local normal vapour flux, j, at the liquid-gas interface: $j = j_{approx}$. All input data required for the computation of j_{approx}, such as T_{av}, $\theta(t)$, and $\mathbf{j}_\tau$ are provided from the computations at previous iteration. Our one-sided model solves for Navier-Stokes, continuity, and heat transfer equations in the droplet bulk

$$\rho \left(\frac{\partial \mathbf{u}}{\partial t} \bigg|_m + [(\mathbf{u} - \mathbf{w}) \cdot \mathbf{V}] \mathbf{u} \right) = \mathbf{V} \cdot \boldsymbol{\sigma}, \qquad (24)$$

$$\mathbf{V} \cdot \mathbf{u} = 0, \qquad (25)$$

$$\rho c_p \left(\frac{\partial T}{\partial t} \bigg|_m + (\mathbf{u} - \mathbf{w}) \cdot \mathbf{V} T \right) = \mathbf{V} \cdot (k \mathbf{V} T), \qquad (26)$$

where $\mathbf{u}$ and T are the velocity and temperature fields, respectively, $\mathbf{w}$ is the mesh velocity, subscript m means that the time derivative is taken at a fixed mesh node (fixed mesh coordinates), ρ, c_p, and k are the density, specific heat capacity at constant pressure, and thermal conductivity of the droplet phase, respectively, $\boldsymbol{\sigma} = -p\mathbf{I} + \boldsymbol{\pi}$ is the total stress tensor, p is the hydrodynamic pressure, and $\boldsymbol{\pi} = \mu(\mathbf{V}\mathbf{u} + (\mathbf{V}\mathbf{u})^{\mathrm{T}})$ is the viscous stress tensor. Radiative, conductive, and convective heat transfer into gas phase is neglected. The substrate is considered isothermal with constant temperature T_s. Initial conditions: $T|_{t=0} = T_s$, $\mathbf{u}|_{t=0} = 0$, $p|_{t=0} = p_g + 2\gamma \sin\theta_0 / L$, where γ is the liquid-gas interfacial tension and θ_0 is the initial contact angle. Boundary conditions: $T|_{z=0} = T_s$, $\mathbf{u}|_{z=0} = 0$. The liquid-gas interface Γ is considered as a boundary, moving in the direction of normal vector $\mathbf{n}$ with velocity u_Γ. Provided that the local evaporation rate is known [see Eq. (9)], one can define the boundary conditions at Γ as follows:

$$-k\mathbf{V} T \cdot \mathbf{n} = j\Lambda^* / M_v, \qquad (27)$$

$$\rho(\mathbf{u} \cdot \mathbf{n} - u_\Gamma) = j, \qquad (28)$$

$$\boldsymbol{\sigma} \cdot \mathbf{n} = -\gamma(\mathbf{V} \cdot \mathbf{n})_\Gamma \mathbf{n} + \frac{d\gamma}{dT} \mathbf{V}_\Gamma T, \qquad (29)$$

where $(\mathbf{V} \cdot \mathbf{n})_\Gamma$ is the divergence of vector $\mathbf{n}$ at Γ, that is the curvature of Γ, which is equal to $2\sin\theta / L$. Expression for u_Γ is derived based on total evaporative mass flux $J = \int_\Gamma j d\Gamma$ and two assumptions: pinned contact line ($L = const$) and spherical-cap shape of the droplet in the course of evaporation

$$u_\Gamma = -\frac{J}{\pi\rho L^3} \frac{(1 + \cos\theta)^2}{\sin\theta} z. \qquad (30)$$

To model the sessile droplet evaporation process, the location of the liquid-vapour interface is unknown to be determined. Moreover, as it moves in time, the mesh on which is discretised the governing equations must dynamically fit the moving boundary. To this end, an Arbitrary Lagrangian-Eulerian (ALE) formulation is used to solve the time dependent problem on a computational domain that matches the moving interface. Therefore, a mesh velocity (denoted w) appears in momentum [Eq. (24)] and heat [Eq. (27)] transport equations. The mesh deforms in such a way to follow the moving boundary of the computational domain, and so, it approaches closer and closer to the substrate due to the evaporation process. The droplet surface velocity u_{Gamma} is given by Eq. (31).

In order to compare our numerical model with experimental data, we have selected one particular experiment from our series of parabolic-flight experiments.[17] The selected configuration is a sessile droplet of ethanol with a pinned contact line that evaporates in microgravity conditions from a thin heated substrate with an actively imposed constant temperature T_s. The input data related to the selected case are the following: $p_g = 792$ mbar, $T_s = 307.05$ K, $T_\infty = 297.55$ K, $L = 2.95$ mm, $\theta_0 = 29.2°$, $\rho_{v,\infty} = 0$, $\rho = 772.24$ kg/m^3, $\mu = 1.095$ mPa $\cdot$ s, $k = 0.14$ W/(mK), $c_p = 2602.3$ J/(kg K), $\gamma = 20.62$ mN/m, and $\frac{d\gamma}{dT} = -82\mu$ N/(mK). Parameters $B = 0.33$ K^{-1} and $\Delta h = 0.019$ mm in Eq. (9) were obtained by fitting the local evaporation rate (j), computed with our previously developed non-isothermal two-sided axisymmetric numerical model,[26] which also uses the same input data.

The governing equations have been implemented using the COMSOL Multiphysics® software, discretized with the finite element method (FEM) using second order shape functions. An optimized mesh has been built on 16 547 tetrahedral elements (resulting in 187 050 degrees of freedom) so that computations ran for about 9 days on a cluster with 48 cores. Computations start with a uniform initial temperature field (at substrate heating temperature) in the droplet and the imposed heating temperature at the substrate surface. Due to the latent heat of vaporization, the droplet cools down from the liquid-gas interface; meanwhile, temperature near the contact line remains higher due to heat conduction from the substrate through a thin layer of ethanol. This creates a vertical temperature gradient in the droplet bulk and a tangential one along the droplet surface near the contact line. These temperature gradients promote the development of thermocapillary Benard-Marangoni instability. After intense unsteady phenomena finished (at about $t = 5$ s), one can observe a dynamic multicellular thermo-convective pattern: Fig. 1 (Multimedia view) shows the temperature (color) and velocity (arrows) fields in the vertical median plane [(a) (Multimedia view)] and at the droplet interface [(b) (Multimedia view)] at about 85% of the total time of evaporation ($t = 15.4$ s). The dynamics of this instability well resembles the experimentally observed one. So, as the present computations enable us to access the transient internal fluid flow structure inside the evaporating droplet, let us now detail how such 3D instabilities develop over time.
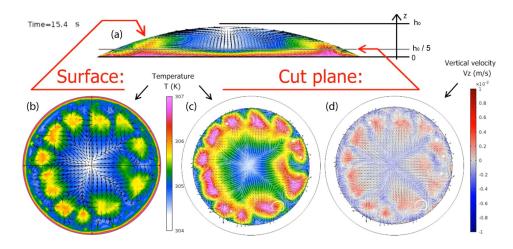
FIG. 1. Snapshot of flow motion inside the droplet under evaporation from the numerical simulation at $t = 15.4$ s. (a) Thermal plume formation in the droplet vertical median plane. (b) Interfacial temperature. (c) Liquid temperature in a horizontal cut plane ($z = h_0/5$). (d) Vertical velocity component in a horizontal cut plane ($z = h_0/5$). Multimedia view: https://doi.org/10.1063/1.5006707.1

In the first stage, an unsteady axisymmetric base flow sets up in a torus roll adjacent to the contact line. It rotates upwards along the interface as it is driven by thermo-capillary forces and superimposes to Stefan flow in the droplet. In the second stage, this torus roll is destabilized and brakes into several BM cells resulting in a fully 3D unsteady pattern that populates the whole droplet. Then, in the third stage, the BM cells move toward an outer ring close to the contact line where thermo-capillary forces remain much more intense than in the apex region of low thermal gradients. The transient pattern that arises from this point results from the fact that BM cells have an intrinsic wavelength that is roughly twice the local liquid thickness[30] [i.e., $\lambda \sim 2$ f(r)]. So, the number of BM cells which matches the circumference is $N(t) \sim \frac{\pi(L - f(r))}{f(r)}$. However, as evaporation proceeds in the pinned mode, the droplet thickness decreases and N(t) increases, leading to a continuous azimuthal movement in order to evenly distribute cells along the droplet perimeter.

This last dynamics has undoubtedly been erroneously attributed to HTWs, but they are actually BM instabilities. Indeed, the internal flow structure in the droplet reveals that there is no base shear flow directed along the tangential thermal gradient along the interface, basic condition to be satisfied for HTWs to appear according to Refs. 19,20,24, and 25. Therefore, these experimentally observed thermo-convective instabilities cannot be classified as HTWs but actually unsteady Benard-Marangoni instabilities.

In order to get quantitative observable comparisons between computations and experimental results, we post-processed simplified IR images based on the computed temperature field. Experimental IR was recorded from the droplet top view with a camera "VarioCam® hr head" in the mid-wavelength IR range [MW: 7.5–14 μm; Fig. 2(c) (Multimedia view)]. For the numerical IR post-processing, we took into account the semi-transparency of liquid ethanol in the mid-wavelength (MW) bandwidth: according to the spectrophotometer measurements by Brutin *et al.*,[13] ethanol's absorption coefficient in the MW range is $a = 1.85$ mm^{-1}. Using this value, one can compute the intensity of IR radiation arriving to the camera installed above the droplet, which then can be converted into an equivalent blackbody temperature, $T_{IR,num}(x, y)$ (subscript *num* stands for "numerical"). This computation is done by summing the IR radiation coming from the substrate surface (assumed to be a gray body) with

the integral of IR radiation sources distributed across the thickness of a semi-transparent droplet

$$T_{IR,num}^4(x,y) = \varepsilon T_s^4 e^{-af(x,y)} + \int_0^{f(x,y)} T^4(x,y,z) a\, e^{-a(f(x,y)-z)}\, dz, \quad (31)$$

where $f(x, y)$ represents the local droplet thickness. The emissivity of a bare substrate surface, $\varepsilon = T_{IR,\,\mathrm{exp}}^4 / T_{s,\,\mathrm{exp}}^4$, is estimated by correlating the experimental equivalent blackbody temperature [$T_{IR,\,\mathrm{exp}}(x, y)$ from IR camera] with the corresponding real temperature, $T_{s,\,\mathrm{exp}}$, obtained through thermocouple measurements.

The quantitative agreement between computed IR [Fig. 2(b) (Multimedia view)] and experimental one [Fig. 2(c) (Multimedia view)] confirms that our one-sided model has been able to catch the main dynamics of the droplet evaporating process, and it is able to faithfully reproduce it. In this
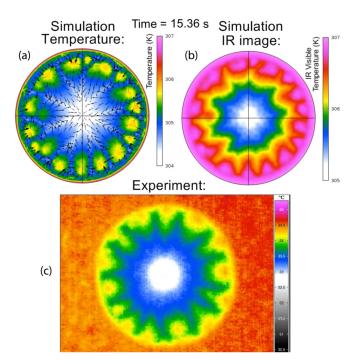

FIG. 2. Snapshot of computed and experimental infrared images of an evaporating ethanol droplet at $t = 15.36$ s. (a) Computed droplet surface temperature. (b) Computed droplet total radiative temperature. (c) Experimental infrared image. Multimedia view: https://doi.org/10.1063/1.5006707.2

paper, we have reported our 3D one-sided numerical model of an evaporating sessile droplet of ethanol on a heated substrate. The model does not use any fitting parameters and demonstrates a good qualitative and quantitative comparison with the experimental data. Based on the computed temperature and flow fields, we conclude that the experimentally observed thermo-convective pattern in the droplet is an unsteady Benard-Marangoni instability and is different from hydrothermal waves.

[1]P. Boulet, J. Tissot, F. Trinquet, and L. Fournaison, Appl. Therm. Eng. **50**, 1164 (2013).

[2]J. Chen, W.-S. Liao, X. Chen, T. Yang, S. E. Wark, D. H. Son, J. D. Batteas, and P. S. Cremer, ACS Nano **3**, 173 (2009).

[3]J. H. Combellack, Crop Prot. **3**, 9 (1984).

[4]S. H. Ko, J. Chung, N. Hotz, K. H. Nam, and C. P. Grigoropoulos, J. Micromech. Microeng. **20**, 125010 (2010).

[5]N. C. Schirmer, S. Ströhle, M. K. Tiwari, and D. Poulikakos, Adv. Funct. Mater. **21**, 388 (2010).

[6]W. BouZeid and D. Brutin, Colloid Surf. A **430**, 1 (2013).

[7]W. BouZeid, J. Vicente, and D. Brutin, Colloid Surf. A **432**, 139 (2013).

[8]B. Sobac and D. Brutin, Colloid Surf. A **448**, 34 (2014).

[9]S. Dehaeck, A. Rednikov, and P. Colinet, Langmuir **30**, 2002 (2014).

[10]K. Sefiane, J. R. Moffat, O. K. Matar, and R. V. Craster, Appl. Phys. Lett. **93**, 074103 (2008).

[11]K. Sefiane, A. Steinchen, and R. Moffat, Colloid Surf. A **365**, 95 (2010).

[12]D. Brutin, Z.-Q. Zhu, O. Rahli, J.-C. Xie, Q.-S. Liu, and L. Tadrist, Microgravity Sci. Technol. **22**, 387 (2010).

[13]D. Brutin, B. Sobac, F. Rigollet, and C. L. Niliot, Exp. Therm. Fluid Sci. **35**, 521 (2011).

[14]B. Sobac and D. Brutin, Phys. Fluids **24**, 032103 (2012).

[15]K. Sefiane, Y. Fukatani, Y. Takata, and J. Kim, Langmuir **29**, 9750 (2013).

[16]B. Sobac, "Evaporation de gouttes sessiles: des fluides purs aux fluides complexes," Ph.D. thesis, Aix-Marseille University, 2012.

[17]F. Carle, B. Sobac, and D. Brutin, J. Fluid Mech. **712**, 614 (2012).

[18]D. Brutin, F. Carle, and F. Rigollet, "Radiative heat transfer in droplets," in *Droplet Wetting and Evaporation* (Academic Press, USA, 2015), pp. 193–199.

[19]M. K. Smith and S. H. Davis, J. Fluid Mech. **132**, 119 (1983).

[20]M. K. Smith and S. H. Davis, J. Fluid Mech. **132**, 145 (1983).

[21]N. Garnier, A. Chiffaudel, and F. Daviaud, "Hydrothermal waves in a disk of fluid," in *Dynamics of Spatio-Temporal Cellular Structures* (Springer-Verlag, New York, 2006), p. 147.

[22]P. J. Saenz, P. Valluri, K. Sefiane, G. Karapetsas, and O. K. Matar, Phys. Fluids **25**, 094101 (2013).

[23]D. Schwabe, A. Zebib, and B.-C. Sim, J. Fluid Mech. **491**, 239 (2003).

[24]M. K. Smith, Phys. Fluids **29**, 3182 (1986).

[25]F. H. Busse and S. C. Müller, *Evolution of Spontaneous Structures in Dissipative Continuous Systems* (Springer Science and Business Media, Berlin, 1998).

[26]S. Semenov, F. Carle, M. Medale, and D. Brutin, "Boundary conditions for a one-sided numerical model of evaporative instabilities in sessile drops of ethanol on heated substrates," Phys. Rev. E. (to be published).

[27]R. G. Picknett and R. Bexon, J. Colloid Interf. Sci. **61**, 336 (1977).

[28]Y. O. Popov, Phys. Rev. E **71**, 036313 (2005).

[29]R. C. Reid and T. K. Sherwood, *The Properties of Gases and Liquids* (McGraw-Hill, New York, 1958).

[30]M. Medale and P. Cerisier, Eur. Phys. J. Spec. Top. **224**, 217 (2015).